Biogeosciences Discuss., 12, 7739–7781, 2015
www.biogeosciences-discuss.net/12/7739/2015/
doi:10.5194/bgd-12-7739-2015

Biogeosciences Discussions Open Access

Wind-driven interannual variability of sea ice algal production over the western Arctic Chukchi Borderland

E. Watanabe[1], J. Onodera[1], N. Harada[1], M. N. Aita[1], A. Ishida[2], and M. J. Kishi[3]

[1]Japan Agency for Marine-Earth Science and Technology, Yokosuka, Japan
[2]Department of Social and Environmental Studies, Tokoha University, Fuji, Japan
[3]School of Fisheries Sciences, Hokkaido University, Hakodate, Japan

Received: 23 April 2015 – Accepted: 29 April 2015 – Published: 22 May 2015

Correspondence to: E. Watanabe (ejnabe@jamstec.go.jp)

Published by Copernicus Publications on behalf of the European Geosciences Union.

Abstract

Seasonal and interannual variability in sinking flux of biogenic particles was reported by the multi-year bottom-tethered sediment trap measurements in the Northwind Abyssal Plain (Station NAP: 75° N, 162° W, 1975 m water depth) of the western Arctic Chukchi Borderland. Whereas the trapped particle flux had an obvious peak with the dominance of sea ice-related diatom valve in August 2011, the observed particle flux was considerably suppressed throughout the summer season in 2012. In the present study, the response of ice algal production and biomass to wind-driven changes in physical environments was addressed using a pan-Arctic sea ice–ocean modeling approach. Sea ice ecosystem with ice algae was newly incorporated into the lower-trophic marine ecosystem model, which was previously coupled with a high-resolution (i.e., horizontal grid size of 5 km) ocean general circulation model. Seasonal experiments covering two year-long mooring periods indicated that primary productivity of ice algae around the Chukchi Borderland depended on basin-scale wind pattern through various processes. Easterly wind in the southern part of distinct Beaufort High supplied high abundance of nutrients for euphotic zones of the NAP region via both surface Ekman transport of Chukchi shelf water and vertical turbulent mixing with underlying nutricline water as in 2011. In contrast, northwesterly wind flowing in the northern part of extended Siberian High transported oligotrophic water within the Beaufort Gyre circulation toward the NAP region as in 2012. The modeled ice algal biomass during the summer season certainly reflected the differences in nutrient distribution. The sinking flux of Particulate Organic Nitrogen (PON) was comparable with the time series obtained from the sediment trap data in summer 2011. On the other hand, lateral advection of shelf-origin ice algal patch during a great cyclone event might have caused a model bias on the PON flux in 2012. The extension of year-long measurements is expected to help the illustration of more general features on the Arctic marine biological pump.

1 Introduction

Response of biogeochemical cycle to the Arctic sea ice decline has become an important topic for a variety of communities. The improved light condition in summer has enhanced photosynthesis activity of phytoplankton in the Eurasian pelagic area of the Arctic Ocean (Wassmann, 2011). A widespread massive deposition of ice algal biomass was detected on the deep seafloor of eastern Arctic basin (Boetius et al., 2013). On the other hand, the under-ice export of particulate organic carbon was limited by insufficient nutrient supply in the stratified central Arctic (Lalande et al., 2014). In the Beaufort Gyre region of western Arctic, the freshwater accumulation suppressed the primary production of phytoplankton during the 2000s (McLaughlin et al., 2010; Nishino et al., 2011). It is still necessary to further fill many gaps to understand the spatial and temporal variability of biological processes in the Arctic Ocean.

Sediment trap measurement is a useful tool to capture year-long signals of biological activity. The location of bottom-tethered traps has been however confined to north of Laptev Sea (Fahl and N thig, 2007), Mackenzie shelf (Forest et al., 2007), and the deep Canada Basin (Honjo et al., 2010). In our field campaign, the year-round bottom-tethered moorings with sediment trap instrument have been deployed in the Northwind Abyssal Plain (NAP) of Chukchi Borderland since October 2010 (Fig. 1). At Station NAP (75° N, 162° W, 1975 m water depth), early-winter maxima of sinking particle flux with fresh organic material were captured every year (Watanabe et al., 2014; Onodera et al., 2015). The substantial amount of lithogenic minerals in the trapped particle reminded of shelf-origin water transport toward the NAP region. Seasonal experiments using an eddy-resolving (5 km grid size) pan-Arctic sea ice–ocean model indicated the effective role of Beaufort shelf-break eddies in transport of the Chukchi shelf water with high biological productivity and in the consequent early-winter peaks of sinking biogenic flux at Station NAP (Watanabe et al., 2014). It should be noted that biological activity could continue during eddy migration inside the Canada Basin.

Another finding obtained at Station NAP was remarkable interannual variability in the summertime particle flux (Onodera et al., 2015; Ikenoue et al., 2015; Matsuno et al., 2015). The trapped particle flux had its sharp peak in August 2011 and was considerably suppressed in summer 2012. The relative abundance of diatom valves suggested the dominance of oligotrophic water originating from the central Canada Basin in 2012. This situation was supported by ocean current fields demonstrated in a medium-resolution (25 km grid size) framework of the pan-Arctic physical oceanographic model (Onodera et al., 2015). However, the reliable in-situ data of biological productivity and water mass transport above the shallow trap depth (approximately 180–260 m) were insufficient during the mooring periods. Further investigation on more detailed background mechanisms for summertime biogenic flux is highly valuable. Whereas the major content of observed diatom valves was sea ice-related species *Fossula arctica* (Onodera et al., 2015), sea ice ecosystem was not included in our previous model experiment (Watanabe et al., 2014). The lack of ice algae was a plausible factor for the summertime delay of simulated biogenic flux peak behind the trap data.

There was long history of ice algae model development. A pioneer work was conducted for the Antarctic fast ice ecosystem (Arrigo et al., 1993). In the Arctic Ocean, a one-dimensional ice algae model was applied to landfast ice in the Resolute Passage of Canadian Archipelago (Lavoie et al., 2005; Pogson et al., 2011) and offshore Barrow (Jin et al., 2006). In the recent years, the target region has been extended to the whole Arctic Ocean (Dupont, 2012) and global domain (Deal et al., 2011; Jin et al., 2012). The analysis period covered from seasonal transition (Lavoie, 2005; Deal et al., 2011) to decadal variability (Jin et al., 2012; Dupont, 2012) and future projection (Lavoie et al., 2010). Most models assumed that ice algal activity occurred primarily in the skeletal layer of sea ice bottom (i.e., ice–water interface), where the layer thickness was fixed to 2 cm (Lavoie et al., 2005), 3 cm (Jin et al., 2012), and 5 cm (Dupont, 2012). The ice algal biomass sometimes reached three orders of magnitude larger at ice–water interface than the upper part of sea ice column (Dupont, 2012). Seawater in the ocean surface column is a major nutrient supplier for ice algae in the skeletal layer. The tidal

mixing controls nutrient exchange rate at ice–water interface in narrow shallow straits of Canadian Archipelago (Lavoie et al., 2005). More generally, it is reasonable that the nutrient flux is calculated as a function of sea ice freezing/melting rate (Jin et al., 2006; Deal et al., 2011). On the other hand, in Dupont (2012), the nutrient import due to sea ice freezing was neglected following an observational view, where nutrient trapped inside sea ice column was not of great importance for ice algal bloom (Cota et al., 1991; Cota and Smith, 1991). The grazing pressure on ice algae was considered to be weak in sea ice column. Most previous models hence excluded zooplankton biology in the skeletal layer (Jin et al., 2006; Dupont, 2012) or prescribed small grazing rate of potential grazers (e.g., amphipods) (Lavoie, 2005). Ice algae lose their habitat due to sea ice melting. The assemblage released from sea ice bottom is converted to detritus and partially seeds pelagic and benthic species in the water column (Michel et al., 1993, 1996). Thus the complex processes of ice algae have been proposed and numerically formulated in various manners.

In the present study, we addressed seasonal and interannual variability of ice algal production and biomass over the Chukchi Borderland using a pan-Arctic ice–ocean modeling approach (Fig. 1). In this effort, to represent the summertime biogenic particle flux captured by sediment trap measurements, sea ice ecosystem was newly incorporated into a lower-trophic marine ecosystem model. Configuration of modeling and sediment trap analyses is described in Sect. 2. Seasonal transitions of the modeled ice–ocean field, especially around the NAP region, are traced in Sect. 3. Relationships of the interannual variability with wind pattern are examined in Sect. 4. The findings obtained in the present work are summarized in Sect. 5.

2 Model configuration and experimental design

2.1 Physical oceanographic model

The physical part of coupled sea ice–ocean model used in the present work is "Center for Climate System Research Ocean Component Model (COCO)" version 4.9 (Hasumi, 2006). The sea ice component includes a multi-thickness-category configuration based on that of Bitz et al. (2001) with a one-layer thermodynamic formulation (Bitz and Lipscomb, 1999), the linear-remapping method for category transfer (Lipscomb, 2001), and the elastic-viscous-plastic rheology (Hunke and Dukowicz, 1997). In addition to open water category, the lower limit of sea ice thickness in each category is set to be 10, 30, 60, 100, 250, and 500 cm, respectively (i.e., 7 category). The ocean component is a free-surface general circulation model formulated with the advection scheme of Leonard et al. (1994) and the turbulence closure mixed-layer scheme of Noh and Kim (1999).

2.2 Marine ecosystem model

The COCO model was coupled with a lower-trophic marine ecosystem model, "North Pacific Ecosystem Model for Understanding Regional Oceanography (NEMURO)". The detailed configuration of original NEMURO model, which represented pelagic plankton species (i.e., diatom, flagellate, and copepod), was described in Kishi et al. (2007). In the present work, to address seasonality and interannual variability of ice algal production and biomass, sea ice ecosystem was additionally incorporated (Fig. 2). In the developed model (called as "Arctic NEMURO", hereafter), the habitat of ice algae is confined to the skeletal layer with its thickness of 2 cm. The biogeochemical variables in sea ice component comprise ice algae (IA), ice-related zooplankton (ZI: neglected in the present experiment), nitrate (NO_3), ammonium (NH_4), silicate (SIL), dissolved organic nitrogen (DON), particulate organic nitrogen (PON), and opal (OPL). Each model grid has a single value per variable independent of ice thickness category. Since sea

ice bottom temperature is always kept at the freezing point of underlying sea water, the growth rate of ice algae (GR) is calculated depending on light condition (L) and nutrient uptake (N_{up}) terms:

$$GR = GR_{max} \times L \times N_{up},$$

where the maximum growth rate GR_{max} is fixed to a constant value of $0.8\,d^{-1}$.

The light condition term followed the original NEMURO formulation:

$$L = I/I_{opti} \times \exp(1 - I/I_{opti}),$$
$$I = PAR_{frac} \times SW^{\downarrow} \times (1 - \alpha_{sfc}) \times \exp(-k_{snow}H_{snow} - k_{ice}H_{ice}),$$

where I is photosynthetically active radiation (PAR) in the skeletal layer. The conversion coefficient from shortwave radiation to PAR (PAR_{frac}) is 0.43 following the previous models (Zhang et al., 2010; Dupont, 2012) so that 43 % of shortwave flux is available for photosynthesis activity. Light transmission through snow and sea ice columns is given by downward shortwave radiation from atmosphere ($SW^{\downarrow}$), snow/ice surface albedo (α_{sfc}), column thickness (H_{snow}, H_{ice}), and empirical extinction rates (k_{snow}, k_{ice}). The surface albedo (α_{sfc}) changes from 0.8 to 0.6 depending on snow/ice type and surface temperature during the summer season. The light extinction rate (k_{snow}, k_{ice}) is set to $0.12\,cm^{-1}$ for snow and $0.045\,cm^{-1}$ for sea ice based on Aota and Ishikawa (1982). The light intensity in the skeletal layer is approximately 10 % (1 %) of that absorbed into the surface of sea ice with its thickness of 50 cm (100 cm) (Fig. 3a). The light transmission is calculated in each thickness category (see the category arrangement in Sect. 2.1), and the under-ice average intensity is then obtained in each model grid. Self-shading effect of ice algae is neglected. For weak-light adaptation of ice algae, the optimal light intensity (I_{opti}) is set to $10\,W\,m^{-2}$ (cf., $104\,W\,m^{-2}$ for pelagic phytoplankton, Kishi et al., 2007). The PAR of 5 and $20\,W\,m^{-2}$ results in the light condition term of 0.82 and 0.73, respectively (Fig. 3b).

The vertical exchange of biogeochemical variables between the skeletal layer and the ocean surface layer (suffixed as SKL and OCN, respectively, hereafter) is formulated in the different manner for sea ice freezing and melting periods. During the freezing period, ocean-to-ice fluxes F_{OI} are proportional to sea ice freezing rate IFR:

$$F_{OI} = CF_{OI} \times (NO_3, NH_4, SIL, DON)_{OCN} \times IFR.$$

The proportional coefficient CF_{OI} is set to 0.3, since first-year ice salinity is able to reach approximately 30 % of ocean salinity. In addition, all of the imported nutrients are concentrated in the skeletal layer under an idealized assumption. There is no import of particles such as pelagic planktons, PON, and OPL. During the melting period, ice-to-ocean fluxes F_{IO} are proportional to sea ice melting rate IMR:

$$F_{IO} = (IA, NO_3, NH_4, SIL, DON, PON, OPL)_{SKL} \times IMR.$$

According to this formulation, the concentration of all biogeochemical variables in sea ice component is reduced to zero when sea ice entirely disappears due to melting process in each model grid. Whereas sea ice melts from its surface, bottom, and flank, respectively, it is difficult to separate these melting processes in terms of particle export. In general, ice surface meltwater sinks through internal brine channels and flushes out a part of materials in the skeletal layer (Pogson et al., 2011). Besides, ice algae have an ability to maintain their position under slow melting rate, and the habitat is not immediately lost even after ice bottom melting. The methods adopted in the present work idealize ice–ocean exchange of biogeochemical variables within reasonable scopes.

There is uncertainty whether direct nutrient source of ice algal growth is positioned in sea ice column or underlying sea water. The present study assumes that ice algae utilize both ice/ocean nutrients depending on their biomass:

$$N_{up} = RN_{upSKL} \times N_{upSKL} + (1 - RN_{upSKL}) \times N_{upOCN},$$
$$RN_{upSKL} = 0.5 \times \{\cos(\pi \times IA/KN_{upSKL}) + 1\}, \text{ for } IA \leqq KN_{upSKL},$$

where RN_{upSKL} is an ice algal uptake ratio of nutrient in the skeletal layer, and KN_{upSKL} is a threshold value (Fig. 3c). When ice algal biomass IA exceeds KN_{upSKL}, only sea water nutrient is utilized for their growth. The value of KN_{upSKL} is set to 1 mmol N m^{-2} in the present experiments. As reported in Sect. 3.2, the ice nutrient is preferentially consumed for initial bloom of small-sized ice algae in early summer. According to the growth of ice algae, their nutrient source shifts to sea water for the mature period. The "hybrid-type" formulation of nutrient uptake represents more realistic ice algal biology, where ice algae anchoring under ice floes gradually raise meter-long filaments in the water column (Boetius et al., 2013). In each model time step, the Michaelis–Menten relationship is applied to nutrient concentration in the skeletal layer and in the ocean surface layer (i.e., the uppermost ocean grid), respectively (Fig. 3d):

$$N_{upSKL} = \min\{NO_{3SKL}/(NO_{3SKL} + K_{NO_3}) \times \exp(-\Psi_{NH_4} \times NH_{4SKL}) + NH_{4SKL}/(NH_{4SKL} + K_{NH_4}), SIL_{SKL}/(SIL_{SKL} + K_{SIL})\},$$

$$N_{upOCN} = \min\{NO_{3OCN}/(NO_{3OCN} + K_{NO_3}) \times \exp(-\Psi_{NH_4} \times NH_{4OCN}) + NH_{4OCN}/(NH_{4OCN} + K_{NH_4}), SIL_{OCN}/(SIL_{OCN} + K_{SIL})\},$$

where the constant coefficients of half saturation for nitrate (K_{NO_3}), ammonium (K_{NH_4}), and silicate (K_{SIL}) and of ammonium inhibition (Ψ_{NH_4}) have the same values as those of pelagic diatoms (i.e., large phytoplankton PL in the NEMURO model) (Kishi et al., 2007).

The biomass of ice algae is reduced by respiration, mortality, zooplankton grazing, and sea ice melting. The respiration and mortality terms are functions of only ice algal biomass itself (under the freezing temperature assumption). In the present experiments, zooplankton biomass of sea ice component (ZI) is kept at zero, and zooplankton grazing on ice algae is neglected. All of ice algae are converted to PON after their export to water column by sea ice melting. In this connection, sea ice assemblage sinks faster than other particles derived from pelagic plankton because the aggregation of ice algae proceeds before the export to water column. ~~The German field campaign de-~~ ~~tected a~~ rapid sinking of ice-related species (~~Boetius et al., 2013~~). The modeled PON is hence divided into two components with different sinking speeds. The sinking speed of PON derived from ice algae and from pelagic plankton ranges from 50 to 200 m d^{-1} and from 2 to 200 m d^{-1}, respectively, following a cosine curve (Fig. 3e). Below 1000 m depth, the sinking speed is maintained at 200 m d^{-1}. These profiles are reasonable because the sinking of particulate organic materials generally accelerates with depths due to particle densification processes (e.g., aggregation in shallow depths and elimination of light/fragile organic materials in middle depths) (Honda et al., 2013). The modeled OPL is treated in the same manner.

Since the Arctic NEMURO is implemented in three-dimensional frameworks, the horizontal advection of biogeochemical variables in sea ice component is also calculated. The divergence (convergence) of sea ice velocity causes loss (accumulation) of each material as well as snow and ice volumes. Whereas actual ridging process is accompanied by complex deformation, the modeled sea ice ecosystem is consistently kept in the skeletal layer with its constant thickness of 2 cm for simplicity.

2.3 Experimental design

The model domain contains the entire Arctic Ocean, the Greenland-Iceland-Norwegian (GIN) seas, and the northern part of the North Atlantic (Fig. 1). The horizontal resolution is 5 km. There are 42 hybrid σ-z vertical levels. The vertical grid width varies from 2 m at the top level to 500 m at the bottom level. The σ-coordinate composed of three levels is applied in the uppermost 10 m. We performed two one-year experiments, where the 5 km grid model was integrated from October 2010 (2011) to September 2011 (2012) ~~in the 2011 (2012) case~~ to examine the seasonal and interannual variability of ice algae. The initial sea ice and ocean physical fields for these experiments were obtained from the decadal experiment from 1979 to 2011 using the 25 km grid version (Onodera et al., 2015). The atmospheric forcing components were constructed from the National Centers for Environmental Prediction/Climate Forecast System Reanalysis (NCEP/CFSR) 6 hourly dataset (Saha et al., 2010). At the Bering Strait, Pacific wa-

ter inflow with a seasonal cycle was prescribed. Monthly climatological data of nitrate and silicate concentrations derived from the World Ocean Atlas 2013 (WOA13) (Garcia et al., 2013) were used for restoring along the lateral boundary region of the model domain, and the summertime climatology was assigned to the initial fields of ocean nutrient. Since geochemical dissolution from sea bottom sediments is a crucial nutrient source over the Arctic shelves, the fluxes of ammonium, DON, and silicate were added to the deepest layers just above the shelf bottom as in Watanabe et al. (2014). In the skeletal layer, sea ice nutrient is initially zero, and the lower limit of ice algal concentration (0.02 mmol N m^{-3}) is given for seeding.

2.4 Sediment trap analysis

The bottom-tethered sediment traps (SMD26S-6000, NiGK Cooperation) have been moored at Station NAP (75° N, 162° W, 1975 m water depth) since October 2010. The deployment and turnaround were conducted by the Japanese R/V *Mirai* and the Canadian Coast Guard Ship Sir Wilfrid Laurier. In the first year from 4 October 2010 to 27 September 2011, sinking particle sampling was conducted at the depth of 181–218 m (median: 184 m). In the second year from 4 October 2011 to 17 September 2012, the trap depth was 247–319 m (median: 256 m). These sediment traps collected 26 samples approximately every two week during one-year deployment. The trapped particles were evenly divided into 10 samples. The one of 10 aliquot samples was filtered, and the dried one was well grinded and mixed by agate mill. Before the PON analysis, the powdered samples were decalcified in vapour of hydrochloric acid in desiccator for eight hours. Sodium hydroxide pellets were then put in desiccator to neutralize the samples. The PON content in the treated samples was sequentially analysed by the CHN analyser (NCS2500, Thermo Quest). The sinking PON flux was calculated based on PON content, sampling period, opening area of sediment trap (0.5 m^2), and aliquot size of the treated sample (1/10). The detailed analysis method and diatom valve fluxes were described in Onodera et al. (2015). The structures of radiolarian and

copepod captured by the same traps were reported in Ikenoue et al. (2015) and Matsuno et al. (2015), respectively.

3 Seasonal transition over the Chukchi borderland

3.1 Physical environments

We defined the NAP region enclosed by 74–76° N and 159–165° W for following analyses (Fig. 1). Monthly mean values of the NCEP/CFSR cloud fraction, downward shortwave radiation, wind speed at the height of 10 m, snow depth, sea ice thickness, and sea ice concentration averaged in the NAP region were summarized in Table 1. The modeled physical variables was then checked (Fig. 4). In both the 2011 and 2012 cases, the NAP region was entirely covered by sea ice during the winter and spring seasons from December to April, and sea ice concentration gradually decreased from May to September (Fig. 4a). The area-mean sea ice thickness reached approximately 200 cm in April (Fig. 4b), which was a typical value north of the Chukchi Sea (Haas et al., 2010). The declines of sea ice concentration and thickness was consistent with the sea ice melting period from May to September (Fig. 4c). The mechanical divergence of sea ice flow fluctuated within the range of $\pm 0.2 d^{-1}$ in early winter and late summer (Fig. 2d).

Compared with sea ice conditions in the 2011 case, the early-winter covering of sea ice was somewhat delayed in the 2012 case. Although sea ice melting continued until mid-November, the winter sea ice thickness became larger in the 2012 case. The anomalous wind pattern could account for thicker ice transport toward the NAP region, as suggested in Sect. 4.1. The negative anomaly of sea ice thickness in the 2011 case additionally attributed to two melting events in November and December (Fig. 4c) and blanket effect of more snow accumulation on the top of sea ice (not shown). The faster rate of sea ice decline caused earlier sea ice opening in the 2012 case (Fig. 4a and b), partly owing to lower surface albedo with less snow cover. These snow and sea

ice differences were compatible with the NCEP/CFSR data (Table 1). In addition, the enhanced mechanical divergence of sea ice flow from mid-July to August has accelerated the sea ice reduction in 2012 (Fig. 4d). The ice algal biomass in the specific region could be changed by sea ice divergence events. The detailed processes associated with cyclone activities will be discussed in Sect. 4.3.

Since the primary production of ice algae highly depends on nutrient condition in the underlying ocean surface layer, the replenishment of nitrate and silicate from nutricline depths in the water column is substantially important. For the analysis, the Ekman upwelling and downwelling velocity was calculated from the modeled ocean surface stress fields (i.e., the combination of wind stress in open water area and ice–ocean stress under sea ice cover). During the winter period, the week-long Ekman downwelling occurred in both the cases as usually seen inside the Beaufort Sea (Yang, 2009), and the strong upwelling event appeared in the 2011 case (Fig. 4e). In July–August, the sign of Ekman velocity was opposite between two cases. It would be considered that the mid-summer Ekman downwelling (upwelling) played a role in nutricline deepening (shoaling) in the 2011 (2012) case. The vertical turbulent mixing was characterized by vertical diffusivity diagnosed using the closure scheme of Noh and Kim (1999) in the present model. It was shown that the turbulent mixing was activated during the winter season in the 2011 case (Fig. 4f). In the other periods, the smaller values of modeled vertical diffusivity by one or two orders indicated that mixing process had a relatively minor impact on nutrient entrainment in the NAP region. The summertime stratification with sea ice meltwater has been suggested to delay ice algal growth (Michel et al., 1996; Pogson et al., 2011).

3.2 Ice algal production

The modeled primary production of ice algae demonstrated remarkable spatial and interannual variability in the western Arctic Ocean (Fig. 5). Whereas the annual production exceeded 0.6 mmol N m^{-2} over the most area of Chukchi Sea shelf, the low productivity below 0.1 mmol N m^{-2} was located in the central Canada Basin. The shelf-

basin contrast of ice algal production was previously detected by the trans-Arctic Ocean expedition operated in the 1990s (Gosselin et al., 1997). In the 2011 case, the local maximum appeared north of the Chukchi and Beaufort shelf breaks (Fig. 5a). On the other hand, the ice algal productivity was considerably suppressed around the Beaufort Gyre region in the 2012 case (Fig. 5b). The negative anomaly widely covered the western Arctic except the coastal shelves and the northern part of Chukchi Borderland (Fig. 5c). Station NAP was located near the shelf-basin boundary and also showed the negative anomaly.

In the NAP region, the modeled ice algal bloom started in June and produced the peak biomass of 0.7 mmol N m^{-2} at the beginning of August in the 2011 case (Fig. 6a). The Hovm ller diagram visualized the vivid shelf-basin contrast along the 75° N line (Fig. 6b). The bloom signal was quite weak inside the Canada Basin. The massive bloom up to 10 mmol N m^{-2} occurred in July over the Chukchi northern shelf to the west of NAP region. When the relationship of 1 mmol N = 1.6 mg Chl was applied as in Watanabe et al. (2012), the modeled shelf biomass was consistent with the range in the Arctic coastal waters estimated in Cota et al. (1991) (10–300 mg Chl m^{-2}). In the 2012 case, the initial bloom timing was delayed by one month and the ice algal biomass was clearly smaller compared with the 2011 case (Fig. 6a and c). As introduced in Sect. 2.2, the primary production rate of ice algae was calculated using the empirical functions of light condition and nutrient uptake terms. The light condition in the skeletal layer of sea ice column was slowly recovered after the end of polar night (February in the NAP region) and was then rapidly improved by the snow/ice thinning in May (Fig. 7a). The peak value of PAR (3.5 W m^{-2} in the 2011 case, and 2.2 W m^{-2} in the 2012 case) was recorded in mid-July after the summer solstice. Even though sea ice melting continued until September, the light intensity turned to decrease in accordance with the annual cycle of solar radiation. Since the optimal light intensity for ice algal growth (I_{opt}) was set to 10 W m^{-2} in the present experiments, the light condition term varied in phase with the PAR transition (Fig. 7b). The weaker summer light intensity in the 2012 case could attribute to the depressed shortwave radiation with more cloud cover (Table 1),

in spite of thinner sea ice in August (Fig. 4b). The cyclone impact on light condition will be described in Sect. 4.3.

The nutrient condition in the sea ice and water columns showed remarkable interannual variability. The sea ice nitrate content reached the peak value of 0.6 mmol N m^{-2} (0.2 mmol N m^{-2}) in the 2011 (2012) case (Fig. 8a). This amount was an order of magnitude smaller than landfast ice one in the Resolute Passage of Canadian Archipelago (Cota and Smith, 1991). Potential factors for the difference included nutrient environment in the underlying water column and sea ice freezing rate, because the nutrient accumulation in the skeletal layer was induced by ocean-to-ice flux during sea ice freezing period (see the formulation in Sect. 2.2). In the beginning period of one-year model integration, the nutricline was located at the depth of 20 m in the NAP region (Fig. 8b and c). The early-winter Ekman downwelling contributed to nutricline deepening in both the cases (Fig. 4e). In the 2011 case, the Ekman upwelling was also evident in November. However, the duration was just one week so that the Ekman contribution with its peak of 0.8 m d^{-1} played a minor role in the nutrient entrainment. More important key process was the occurrence of strong mixing during the winter season in the 2011 case, as shown in the enhanced vertical diffusivity (Fig. 4f). The resultant surface nitrate concentration increased up to 2 mmol N m^{-3} (Fig. 8b), and the significant part was imported to the skeletal layer of sea ice bottom (Fig. 8a). In contrast, the oligotrophic water stayed over the nutricline whose depth was nearly constant or somewhat deepened for the winter time in the 2012 case (Fig. 8c). The sea ice nitrate content had to reflect the ocean surface value below 1 mmol N m^{-3}. The sea ice silicate, which had a similar difference to nitrate, was not a limiting factor for ice algal growth in the NAP region (not shown). The sea ice freezing rate also differed between two cases. The total amount of thermal sea ice growth from October to April was 160 (136) cm in the 2011 (2012) case. Accordingly, the model results suggested that the preconditioning of nutrient accumulation in the sea ice column during the freezing period controlled the initial bloom of ice algae. The influence of basin-scale wind pattern and water mass transport on nutrient environment will be analyzed in Sect. 4.

The nutrient availability for primary production of ice algae certainly reflected the difference in the above-mentioned precondition. The present model formulated that sea ice nutrient was primarily consumed for the initial stage of ice algal bloom and that the matured ice algae could utilize nutrients in the ocean surface layer. According to the ice algal growth (Fig. 6a), the uptake ratio of sea ice nutrient (RN_{upSKL}) shifted from 1 to 0.7 within a few weeks of July in the 2011 case (Fig. 7c). When the half-saturation constant for nitrate uptake (K_{NO_3}) was set to 6 mmol N m^{-3} for ice algae as well as pelagic diatoms (PL in the present model), the nitrate uptake term before the ice algal bloom was approximately 0.9 (0.7) in the 2011 (2012) case (Fig. 7d). By multiplying the light condition term (Fig. 7b), the growth ratio between two cases became 1.8 at the beginning of June. The larger growth rate accounted for the earlier initial bloom of ice algae in the 2011 case (Fig. 6a). The sea ice nitrate was rapidly depleted by this initial bloom and partially by the export to water column with sea ice melting (Fig. 8a). The following decrease in the RN_{upSKL} value represented the utilization of underlying sea water nutrients (Fig. 7c). The further bloom then occurred in late July (Fig. 6a). In the 2012 case, the decline of nutrient uptake term lagged behind the 2011 case in accordance with the delay of initial bloom (Fig. 7d). The ocean nutrient uptake term, which had ranged lower values during the ice freezing period, gradually became comparable with the 2011 case. The higher RN_{upSKL} value except in early August however restricted the ocean nutrient uptake in the 2012 case (Fig. 7c).

As expected, the seasonal transition of ice algal biomass was similar to the daily primary productivity (Fig. 9a and b). In the present model experiments, the primary production derived from nutrients in the skeletal layer and in the water column was calculated separately. In the 2011 case, the nutrient source of ice algal bloom transited from sea ice column for the first peak of primary production (23 µmol N m^{-2} d^{-1}) to sea water for the second larger peak of 82 µmol N m^{-2} d^{-1}. Thus the model results indicated that the nutrient imported in sea ice column determined the beginning timing of ice algal bloom and that ocean nutrient had a greater contribution to annual primary production of ice algae. In this regard, the relative contribution of ocean nutrients in the 2012 case

was less than the 2011 case. The peak value of primary production recorded in early August was 35 μmol N m^{-2} d^{-1}.

4 Wind impacts on ice algal variability

To address background mechanisms for the western Arctic ice algal variability on the seasonal to interannual timescales, sea ice and ocean responses to wind forcing were investigated.

4.1 Wind and sea ice patterns

The interannual variability in sea ice motion and ocean surface current in the Beaufort Sea is closely related to atmospheric circulation pattern (Yang, 2009; Proshutinsky et al., 2009). We compared the winter mean sea level pressure (SLP) and wind stress fields constructed from the NCEP/CFSR reanalysis data. The wind stress was calculated from the daily mean SLP using the Arctic Ocean Model Intercomparison Project (AOMIP) protocol (http://www.whoi.edu/page.do?pid=30576). In the winter season of 2010–2011, anti-cyclonic wind pattern was accompanied by the weak Beaufort High around the Canada Basin (Fig. 10a). The easterly wind in the southern Beaufort Sea would have favored the transport of nutrient-rich Chukchi shelf water toward the southern Canada Basin with the NAP region via the Ekman process. On the other hand, in winter 2011–2012, high SLP was extended from Siberian Arctic to the western Arctic Ocean (Fig. 10b). Accordingly, northwesterly wind prevailed in the Beaufort Sea. It is reasonable that the anomalous wind pattern forced southward transport of oligotrophic water mass within the Beaufort Gyre and eventually lessened nutrient availability over the Chukchi Borderland.

The changes in wind pattern were consistent with the modeled physical environments in the NAP region, where several differences between the 2011 and 2012 cases were described in Sect. 3.1. For October–November in the 2012 case, local anti-

cyclonic wind forcing had close relationships with the negative rate of sea ice growth, convergence of sea ice velocity, and Ekman downwelling in the NAP region (Fig. 4c–e). The autumn advection of sea ice floes toward the warm water pool induced the lateral/bottom melting along the marginal ice zone, in spite of the enhanced upward heat flux with cold air intrusion (not shown). The convergence of sea ice velocity increased sea ice thickness via mechanical ridging process, in contrast to sea ice melting occurring during the same period, and induced the continuous Ekman downwelling. When we looked at December–January, the positive anomaly of sea ice thickness was produced by the southward transport of thicker sea ice from the central Arctic in the 2012 case (Fig. 4b). The direction of winter sea ice flow around the NAP region obviously differed between two years (Fig. 10c and d), as previously detected by the satellite-based sea ice motion vectors (Onodera et al., 2015). The distance of sea ice movement exceeded 500 km for two months when sea ice velocity was 10 cm s^{-1}.

4.2 Nutrient and shelf-break tracer distributions

The nutrient precondition before the blooming period of ice algae certainly reflected the wind-driven water mass transport suggested in Sect. 4.1. The spatial distribution of ocean nitrate concentration was characterized by the sharp meridional gradient across the Chukchi and Beaufort shelf breaks (Fig. 11), as captured by a number of ship-based observations (Nishino et al., 2011). The modeled vertical average in the top 30 m reached 10 mmol N m^{-3} in the central Chukchi Sea and was below 1 mmol N m^{-3} in the Canada Basin. As shown in Fig. 8, there was a different tendency of the nitrate content around the NAP region. In the 2011 case, relatively high ~~abundance of~~ nitrate ~~was~~ distributed from the northern shelf of Chukchi Sea to the east of Northwind Ridge along 75° N (Fig. 11a). On the other hand, the shelf-basin contrast of nitrate content was still apparent even in the southern area of Chukchi Borderland in the 2012 case (Fig. 11b).

To explore pathways of shelf-break water mass, a virtual passive tracer was provided along the shelf-basin boundary. We chose the tracer source region sandwiched

by the isobaths of 100 and 200 m. Through each one-year experiment, the tracer value was fixed to one from the ocean surface to 200 m depth in the defined region. The advection and diffusion of tracer in the other regions was calculated as well as sea water temperature and salinity. The modeled distribution in March 2011 indicated that the tracer provided along the shelf-basin boundary region was transported from the Chukchi northern shelf toward the Canada Basin interior. The tracer's northern edge matched the nitrate-rich area in the 2011 case (Fig. 11a). The model result hence indicated that the Ekman transport of Chukchi shelf water, in addition to the energetic turbulent mixing, enhanced nutrient availability for ice algae in the NAP region. Besides the southward spread of shelf-break tracer appeared especially south of the Barrow Canyon along the Alaskan northwestern coast. It has been reported that anti-cyclonic wind around the Beaufort High sometimes drove the up-canyon flow (Itoh et al., 2013). Thus the tracer pathway was closely related to basin-scale wind pattern. To the contrary, in March 2012, the tracer signal was quite weak over the Chukchi Borderland (Fig. 11b). The spread of fresher basin water blocked shelf water intrusion and weakened turbulent mixing. The density stratification plausibly controlled ocean surface mixing since wind speed was comparable on the averages from November to January of the 2011 and 2012 seasons (Table 1). This mechanism was consistent with previous findings, where the mixed layer depth was correlated with hydrographic structure rather than wind forcing in the western Arctic (Peralta-Ferriz et al., 2015). The modeled nitrate distribution and tracer pathway supported that the transport of oligotrophic water from the Canada Basin interior toward the NAP region would be an important factor for the suppressed primary productivity of ice algae in summer 2012.

4.3 Impact of great cyclone activity

In summer 2012, an extreme cyclone event was suggested to be a supplementary factor for drastic sea ice reduction especially in the western Arctic and the consequent record minimum extent of Arctic sea ice (Simmonds and Rudeva, 2012; Zhang et al., 2013). A modeling analysis previously indicated that plankton productivity over

the Chukchi, East Siberian, and Laptev shelves was enhanced by vertical mixing with nutrient replenishment and lateral transport of basin-side plankton biomass during the cyclone storm (Zhang et al., 2014). It is assumed that synoptic cyclone activities have both positive and negative contributions to ice algal production. In the 2012 case, the event-like shoaling of upper part of nutricline was caused by mixing and upwelling processes in the NAP region, where the southern part of great cyclone passed and marginal ice floes were located in early August (Fig. 12a). The modeled vertical diffusivity maintained background values partly because strong density stratification suppressed turbulent mixing until July 2012 (Fig. 4f). During the cyclone event with enlarged wind speed (Table 1), the vertical mixing of nearly 10 $cm^2 s^{-1}$ then reached the depth of 20 m (Fig. 4f). Besides, the Ekman upwelling continued from 15 July to 29 August could have worked on nutricline shoaling of 3.3 m (Fig. 4e). However, this timing of nutrient replenishment overlapped with release of ice algae from the skeletal layer due to active sea ice melting (Fig. 8c), and ice algal production was hardly recovered by these processes. Mechanical divergence of sea ice associated with cyclonic wind fields rather contributed to the reduction of ice algal biomass in the specific region (Fig. 4d). Whereas the outward movement of sea ice floes itself did not intend mortality of ice algae, solar heat absorption into the exposed open water fractions enhanced lateral/bottom melting of sea ice and corresponding ice algal release. The light condition for ice algal growth was also changed by cyclone activities with extensive cloud cover. The NCEP/CFSR reanalysis data showed the depression of solar irradiance in the southern part of cyclone passage, where the early August shortwave flux in 2012 was lower relative to the 2011 one by approximately 20 $W m^{-2}$ (not shown). When no snow cover, sea ice thickness of 50 cm, surface albedo of 0.6 were assumed, the downward shortwave radiation of 100 $W m^{-2}$ leaded the PAR of 4.3 $W m^{-2}$ in the skeletal layer of sea ice column. The negative anomaly of light intensity corresponded to the decrease in the light condition term for ice algal growth by less than 0.1.

4.4 PON flux

The time series of sinking PON flux in the NAP region was compared with the sediment trap data. Following the ice algal bloom, in the 2011 case, the modeled PON flux gradually increased from June and had a peak of 15 $\mu mol\,N\,m^{-2}\,d^{-1}$ at the depth of 180 m in mid-August (Fig. 9c). The flux above 8 $\mu mol\,N\,m^{-2}\,d^{-1}$ continued until the end of model integration (i.e., September). The flux amount underestimated in early summer and became comparable afterward with the trap values. The major component of PON flux was originated from ice algae, as observed in the analysis of diatom valve composition (Onodera et al., 2015). The PON export from skeletal layer to underlying water column caused by sea ice melting took approximately 17 $\mu mol\,N\,m^{-2}\,d^{-1}$ during mid-summer. The 67 % of surface flux remained before its dissolution to DON and ammonium at the shallow trap depth of 180 m in August. The comparison with primary production rate suggested that more than half of the organic nitrogen was remineralized in the sea ice column (Fig. 9a and c). The PON flux derived from pelagic phytoplankton and zooplankton gradually increased in August and reached the peak value of 6 $\mu mol\,N\,m^{-2}\,d^{-1}$ in early September. Although the total biomass of pelagic plankton groups was an order of magnitude larger than the ice algal biomass (not shown), the dominance of ice-derived PON for the sinking flux was associated with its faster sinking speed (Sect. 2.2 and Fig. 3e). The sediment trap data captured another peak of PON flux in May 2011. Neither spring bloom of ice algae or pelagic phytoplankton was expected for the sake of thick ice cover in the NAP region. This event might be caused by shelf water transport with lithogenic materials of sea bottom sediments. A candidate driver was the cold-core eddy generated a narrow jet along the Chukchi shelf break (Spall et al., 2008; Lilinas, 2009). The background mechanisms for the spring peak are out of scopes in the present study and will be analyzed as a future work.

The PON flux in the 2012 case produced a distinct mid-summer peak at the ocean surface and the depth of 180 m, although the trapped sample volume was too low to estimate nitrogen content in summer 2012 (Fig. 9d). Most of the modeled PON flux

was the ice-derived one-again. The enhanced sea ice melting up to 4 $cm\,d^{-1}$ assisted the flux peak in early August (Fig. 4c). However, the surface flux remarkably larger than the primary production rate of ice algae, indicated that one-dimensional sea ice processes could not account for the PON flux in the NAP region (Fig. 9b and d). We then traced lateral advection of ice algal biomass around the Chukchi Borderland. In the 2012 case, westerly wind intensified in the southern part of cyclone passage transported shelf-origin ice algal patch toward the Northwind Ridge. Each sea floe could be moved approximately 150 km for 3–10 August. It was plausible that the peculiar advection caused a sudden elevation of ice algal biomass and the overestimation of modeled PON flux in the NAP region (Figs. 6a and 12b). The local biases on sea ice velocity possibly arose attributing to atmospheric momentum input and sea ice dynamics. In the present experiments, the conversion from SLP to wind stress field (i.e., the AOMIP protocol referred in Sect. 4.1) was formulated with specific turning angles, which varied depending on geostrophic wind speed (Proshutinsky and Johnson, 1997). The uncertainties in the reanalysis SLP data should also be paid attention, because the maximum strength of great cyclone in August 2012 calculated from the data assimilation system depended on number of radiosonde profiles (Yamazaki et al., 2015). The traditional rheology of sea ice internal stress has been developed for climate models with grid spacing much coarser than 10 km and did not guarantee its accuracy of ice floe dynamics especially in the marginal ice zone. Thus the speed and direction of modeled ice algal advection around the Chukchi Borderland might have deviated in August 2012, whereas these biases had less impact on basin-scale sea ice and ocean circulation.

Another concern is the event-like deepening of shallow sediment trap at Station NAP in July 2012 (Onodera et al., 2015). The intensified ocean current sometimes inclines the upper part of bottom-tethered mooring system under storm activities. The anchored sea bottom depth of 1975 m and the deepening of trap depth from 260 to 320 m loaded the inclination angle of approximately 15°. It was reported that the trapping efficiency and particle component were remarkably influenced for the tilting range larger than 30° (Gardner, 1985). If this previous examination could be applied in spite of its differ-

ent trap shape from ours, the tilting of 15° would not have a significant impact on the trapping efficiency. In addition, strong ocean current greater than 10 cm s^{-1} sometimes reduces the trapping efficiency (Baker et al., 1988). However, the modeled horizontal velocity at the trap depths was below 2 cm s^{-1} even during the cyclone event (not shown). It should also be noted that the trapped PON flux was continuously negligible throughout the summer season in 2012, not only for the temporal cyclone event.

We further considered other possible factors for the discrepancy of PON flux between the modeled and trap data. Whereas the present model prescribed the fixed vertical profile of sinking speed (Fig. 3e), actual sedimentation depends on ballast distribution in addition to aggregation and elimination of light/fragile organic materials. When the source region of sea ice and surface water in the NAP region was the central Canada Basin, insufficient amount of ballast particles would have allowed slower sinking of PON (Honjo et al., 2010). The variable sinking speed including ballast particles might improve the model performance on PON flux. It has also been reported that ice algae exported to water column could continue their production activity as well as pelagic diatom behavior, and that a part of ice algae is considered to become a food source of higher-trophic plankton (Michel et al., 1996; Gradinger et al., 2009). The grazed algae should be treated as the slower-sinking PON derived from pelagic species so that this conversion would lessen the PON flux. Besides, the PON derived from phytoplankton and zooplankton possibly has different sinking speed. Thus it should be kept in mind that PON sinking process still remains a lot of uncertainties.

5 Summary

The western Arctic biogeochemical structures were addressed using sea ice–ocean modeling approaches. In the present work, sea ice ecosystem with ice algal activity was newly incorporated into the pelagic-type marine ecosystem model. We assumed that ice algae could utilize nutrients (nitrate, ammonium, and silicate) both in the skeletal layer of sea ice column and in the ocean surface layer (i.e., sea water nutrients).

The ratio of nutrient source varied depending on ice algal biomass. This "hybrid-type" nutrient uptake formulation is expected to represent more realistic characteristics of ice algal biology.

The modeled primary production of ice algae demonstrated noticeable interannual variability as assumed by the previous sediment trap analysis in the NAP region. It was found that the ice algal variability was closely related to the change in pan-Arctic-scale wind pattern. In winter 2010–2011, strong easterly winds around the Beaufort High induced the basin-ward Ekman transport of shelf-origin surface water and vertical turbulent mixing with nutricline shoaling. The higher abundance of nitrate was then distributed in the southern Beaufort Sea and the Chukchi Borderland. On the other hand, in winter 2011–2012, northwesterly wind associated with extension of the Siberian High supplied oligotrophic water within the central Canada Basin toward the northern Chukchi shelf. The ice algal productivity in the NAP region was hence suppressed by a deeper nutricline, in addition to cloud shading of solar irradiance, until early summer.

The modeled summer biogenic particle flux in the NAP region was comparable with the sediment trap data in 2011 and remarkably overestimated in 2012. In summer 2012, lateral advection process should have resulted in the enhanced PON flux, because the flux value at the ocean surface exceeded ice algal production in the same location. During the passage of great cyclone in August, westerly wind intensified in the southern part of cyclone transported shelf-origin ice algal patch toward the NAP region. This cyclone event might have caused the model biases on sea ice motion and resultant biogenic particle flux. The successive observation and model improvement are indispensable to obtain more general findings on the Arctic biological pump processes.

Acknowledgements. This study is supported by the Grant-in-Aid for Scientific Research of Japan Society for the Promotion of Science (JSPS) (KAKENHI 22221003, 26800248, and 15H01736) and the GRENE Arctic Climate Change Research Project. Modeling experiments were executed using Earth Simulator of Japan Agency for Marine-Science and Technology (JAMSTEC).

References

Aota, M. and Ishikawa, M.: On the extinction coefficient of sea ice, Low Temperature Science Series A, 40, 127–135, 1982.

Arrigo, K. R., Kremer, J. N., and Sullivan, C. W.: A simulated Antarctic fast ice ecosystem, J. Geophys. Res., 98, 6929–6946, 1993.

Baker, E. T., Milburn, H. B., and Tennant, D. A.: Field assessment of sediment trap efficiency under varying flow conditions, J. Mar. Res., 46, 573–592, 1998.

Bitz, C. M. and Lipscomb, W. H.: An energy-conserving thermodynamic model of sea ice, J. Geophys. Res., 104, 15669–15677, 1999.

Bitz, C. M., Holland, M. M., Weaver, A. J., and Eby, M.: Simulating the ice-thickness distribution in a coupled climate model, J. Geophys. Res., 106, 2441–2463, 2001.

Boetius, A., Albrecht, S, Bakker, K., Bienhold, C., Felden, J., Fern ndez-M ndez, M., Hendricks, S., Katlein, C., Lalande, C., Krumpen, T., Nicolaus, M., Peeken, I., Rabe, B., Rogacheva, A., Rybakova, E., Somavilla, R., Wenzh fer, F., and RV Polarstern ARK27-3-Shipboard Science Party: Export of algal biomass from the melting Arctic sea ice, Science, 339, 1430–1432, 2013.

Cota, G. F. and Smith, R. E. H.: Ecology of bottom ice algae: II. Dynamics, distributions and productivity, J. Marine Syst., 2, 279–295, 1991.

Cota, G. F., Legendre, L., Gosselin, M., and Ingram, R. G.: Ecology of bottom ice algae: I. Environmental controls and variability, J. Marine Syst., 2, 257–277, 1991.

Deal, C., Jin, M., Elliott, S., Hunke, E., Maltrud, M., and Jeffery, N.: Large-scale modeling of primary production and ice algal biomass within arctic sea ice in 1992, J. Geophys. Res., 116, C07004, doi:10.1029/2010JC006409, 2011.

Dupont, F.: Impact of sea-ice biology on overall primary production in a biophysical model of the pan-Arctic Ocean, J. Geophys. Res., 117, C00D17, doi:10.1029/2011JC006983, 2012.

Fahl, K. and N thig, E.-M.: Lithogenic and biogenic particle fluxes on the Lomonosov Ridge (central Arctic Ocean) and their relevance for sediment accumulation: vertical vs. lateral transport, Deep-Sea Res. Pt. I, 54, 1256–1272, 2007.

Forest, A., Sampei, M., Hattori, H., Makabe, R., Sasaki, H., Fukuchi, M., Wassmann, P., and Fortier, L.: Particulate organic carbon fluxes on the slope of the Mackenzie Shelf (Beaufort Sea): physical and biological forcing of shelf-basin exchanges, J. Marine Syst., 68, 39–54, 2007.

Garcia, H. E., Locarnini, R. A., Boyer, T. P., Antonov, J. I., Baranova, O. K., Zweng, M. M., Reagan, J. R., and Johnson, D. R.: World Ocean Atlas 2013, Volume 4: Dissolved Inorganic Nutrients (Phosphate, Nitrate, Silicate), NOAA Atlas NESDIS, 76, 25 pp., Silver Spring, Maryland, USA, 2013.

Gardner, W. D.: The effect of tilt on sediment trap efficiency, Deep-Sea Res., 32, 349–361, 1985.

Gosselin, M., Levasseur, M., Wheeler, P. A., Horner, R. A., and Booth, B. C.: New measurements of phytoplankton and ice algal production in the Arctic Ocean, Deep-Sea Res. Pt. II, 44, 1623–1644, 1997.

Gradinger, R.: Sea-ice algae: major contributors to primary production and algal biomass in the Chukchi and Beaufort Seas during May/June 2002, Deep-Sea Res. Pt. II, 56, 1201–1212, 2009.

Haas, C., Hendricks, S., Eicken, H., and Herber, A.: Synoptic airborne thickness surveys reveal state of Arctic sea ice cover, Geophys. Res. Lett., 37, L09501, doi:10.1029/2010GL042652, 2010.

Hasumi, H.: CCSR Ocean Component Model (COCO) version 4.0, Center for Climate System Research Report, Univ. of Tokyo, 25, 103 pp., Tokyo, Japan, 2006.

Honda, M. C., Kawakami, H., Watanabe, S., and Saino, T.: Concentration and vertical flux of Fukushima-derived radiocesium in sinking particles from two sites in the Northwestern Pacific Ocean, Biogeosciences, 10, 3525–3534, doi:10.5194/bg-10-3525-2013, 2013.

Honjo, S., Krishfield, R. A., Eglinton, T. I., Manganini, S. J., Kemp, J. N., Doherty, K., Hwang, J., McKee, T. K., and Takizawa, T.: Biological pump processes in the cryopelagic and hemipelagic Arctic Ocean: Canada Basin and Chukchi Rise, Prog. Oceanogr., 85, 137–170, 2010.

Hunke, E. C. and Dukowicz, J. K.: An elastic-viscous-plastic model for sea ice dynamics, J. Phys. Oceanogr., 27, 1849–1867, 1997.

Ikenoue, T., Bjørklund, K. R., Kruglikova, S. B., Onodera, J., Kimoto, K., and Harada, N.: Flux variations and vertical distributions of siliceous Rhizaria (Radiolaria and Phaeodaria) in the western Arctic Ocean: indices of environmental changes, Biogeosciences, 12, 2019–2046, doi:10.5194/bg-12-2019-2015, 2015.

Itoh, M., Nishino, S., Kawaguchi, Y., and Kikuchi, T.: Barrow Canyon volume, heat, and freshwater fluxes revealed by long-term mooring observations between 2000 and 2008, J. Geophys. Res., 118, 4363–4379, doi:10.1002/jgrc.20290, 2013.

Jin, M., Deal, C. J., Wang, J., Shin, K.-H., Tanaka, N., Whitledge, T. E., Lee, S. H., Gradinger, R. R.: Controls of the landfast ice–ocean ecosystem offshore Barrow, Alaska, Ann. Glaciol., 44, 63–72, 2006.

Jin, M., Deal, C., Lee, S. H., Elliott, S., Hunke, E., Maltrud, and M., Jeffery, N.: Investigation of Arctic sea ice and ocean primary production for the period 1992–2007 using a 3-D global ice–ocean ecosystem model, Deep-Sea Res. Pt. II, 81–84, 28–35, doi:10.1016/j.dsr2.2011.06.003, 2012.

Kishi, M. J., Kashiwai, M., Ware, D. M., Megrey, B. A., Eslinger, D. L., Werner, F. E., Noguchi-Aita, M., Azumaya, T., Fujii, M., Hashimoto, S., Huang, D., Iizumi, H., Ishida, Y., Kang, S., Kantakov, G. A., Kim, H., Komatsu, K., Navrotsky, V. V., Smith, S. L., Tadokoro, K., Tsuda, A., Yamamura, O., Yamanaka, Y., Yokouchi, K., Yoshie, N., Zhang, J., Zuenko,Y. I., and Zvalinsky, V. I.: NEMURO – a lower trophic level model for the North Pacific marine ecosystem, Ecol. Model., 202, 12–25, 2007.

Lalande, C., N thig, E.-M., Somavilla, R., Bauerfeind, E., Shevchenko, V., and Okolodkov, Y.: Variability in under-ice export fluxes of biogenic matter in the Arctic Ocean, Global Biogeochem. Cy., 28, 571–583, doi:10.1002/2013GB004735, 2014.

Lavoie, D., Denman, K., and Michel, C.: Modeling ice algal growth and decline in a seasonally ice-covered region of the Arctic (Resolute Passage, Canadian Archipelago), J. Geophys. Res., 110, C11009, doi:10.1029/2005JC002922, 2005.

Lavoie, D., Denman, K. L., and Macdonald, R. W.: Effects of future climate change on primary productivity and export fluxes in the Beaufort Sea, J. Geophys. Res., 115, C04018, doi:10.1029/2009JC005493, 2010.

Leonard, B. P., MacVean, M. K., and Lock, A. P.: The flux-integral method for multi-dimensional convection and diffusion, NASA Tech. Memo, 106679/ICOMP-94-13, NASA, Washington, D.C., 1994.

Lin s, L., Pickart, R. S., Mathis, J. T., and Smith, S. L.: Zooplankton inside an Arctic Ocean cold-core eddy: probable origin and fate, Deep-Sea Res. Pt. II, 56, 1290–1304, 2009.

Lipscomb, W. H.: Remapping the thickness distribution in sea ice models, J. Geophys. Res., 106, 13989–14000, 2001.

Matsuno, K., Yamaguchi, A., Fujiwara, A., Onodera, J., Watanabe, E., Harada, N., and Kikuchi, T.: Seasonal changes in the population structure of dominant planktonic copepods collected using a sediment trap moored in the western Arctic Ocean, J. Nat. Hist., in press, 2015.

McLaughlin, F. A. and Carmack, E. C.: Deepening of the nutricline and chlorophyll maximum in the Canada Basin interior, 2003–2009, Geophys. Res. Lett., 37, L24602, doi:10.1029/2010GL045459, 2010.

Michel, C., Legendre, L., Therriault, J.-C., Demers, S., and Vandevelde, T.: Springtime coupling between ice algal and phytoplankton assemblages in southeastern Hudson Bay, Canadian Arctic, Polar Biol., 13, 441–449, 1993.

Michel, C., Legendre, L., Ingram, R. G., Gosselin, M., and Levasseur, M.: Carbon budget of sea-ice algae in spring: evidence of a significant transfer to zooplankton grazers, J. Geophys. Res., 101, 18345–18360, 1996.

Nishino, S., Kikuchi, T., Yamamoto-Kawai, M., Kawaguchi, Y., Hirawake, T., and Itoh, M.: Enhancement/reduction of biological pump depends on ocean circulation in the sea-ice reduction regions of the Arctic Ocean, J. Oceanogr., 67, 305–314, doi:10.1007/s10872-011-0030-7, 2011.

Noh, Y. and Kim, H. J.: Simulations of temperature and turbulence structure of the oceanic boundary layer with the improved near-surface process, J. Geophys. Res., 104, 15621–15634, 1999.

Onodera, J., Watanabe, E., Harada, N., and Honda, M. C.: Diatom flux reflects water-mass conditions on the southern Northwind Abyssal Plain, Arctic Ocean, Biogeosciences, 12, 1373–1385, doi:10.5194/bg-12-1373-2015, 2015.

Peralta-Ferriz, C. and Woodgate, R. A.: Seasonal and interannual variability of pan-Arctic surface mixed layer properties from 1979 to 2012 from hydrographic data, and the dominance of stratification for multiyear mixed layer depth shoaling, Prog. Oceanogr., 134, 19–53, doi:10.1016/j.pocean.2014.12.005, 2015.

Pogson, L., Tremblay, B., Lavoie, D., Michel, C., and Vancoppenolle, M.: Development and validation of a one-dimensional snow-ice algae model against observations in Resolute Passage, Canadian Arctic Archipelago, J. Geophys. Res., 116, C04010, doi:10.1029/2010JC006119, 2011.

Proshutinsky, A. Y. and Johnson, M. A.: Two circulation regimes of the wind-driven Arctic Ocean, J. Geophys. Res., 102, 12493–12514, 1997.

Proshutinsky, A., Krishfield, R., Timmermans, M.-L., Toole, J., Carmack, E., McLaughlin, F., Williams, W. J., Zimmermann, S., Itoh, M., and Shimada, K.: Beaufort Gyre freshwater reservoir: state and variability from observations, J. Geophys. Res., 114, C00A10, doi:10.1029/2008JC005104, 2009.

Saha, S., Moorthi, S., Pan, H.-L., Wu, X., Wang, J., Nadiga, S., Tripp, P., Kistler, R., Woollen, J., Behringer, D., Liu, H., Stokes, D., Grumbine, R., Gayno, G., Wang, J., Hou, Y.-T., Chuang, H.-Y., Juang, H.-M. H., Sela, J., Iredell, M., Treadon, R., Kleist, D., Delst, P. V., Keyser, D., Derber, J., Ek, M., Meng, J., Wei, H., Yang, R., Lord, S., Dool, H. V. D., Kumar, A., Wang, W., Long, C., Chelliah, M., Xue, Y., Huang, B., Schemm, J.-K., Ebisuzaki, W., Lin, R., Xie, P., Chen, M., Zhou, S., Higgins, W., Zou, C.-Z., Liu, Q., Chen, Y., Han, Y., Cucurull, L., Reynolds, R. W., Rutledge, G., and Goldberg, M.: The NCEP Climate Forecast System reanalysis, B. Am. Meteorol. Soc., 91, 1015–1057, doi:10.1175/2010BAMS3001.1, 2010.

Simmonds, I. and Rudeva, I.: The great Arctic cyclone of August 2012, Geophys. Res. Lett., 39, L23709, doi:10.1029/2012GL054259, 2012.

Spall, M. A., Pickart, R. S., Frantantoni, P. S., and Plueddemann, A. J.: Western Arctic shelf-break eddies: formation and transport, J. Phys. Oceanogr., 38, 1644–1668, 2008.

Steele, M., Morley, R., and Ermold, W.: PHC: a global ocean hydrography with a high-quality Arctic Ocean, J. Climate, 14, 2079–2087, 2001.

Wassmann, P.: Arctic marine ecosystems in an era of rapid climate change, Prog. Oceanogr., 90, 1–17, 2011.

Watanabe, E., Kishi, M. J., Ishida, A., and Aita, M. N.: Western Arctic primary productivity regulated by shelf-break warm eddies, J. Oceanogr., 68, 703–718, doi:10.1007/s10872-012-0128-6, 2012.

Watanabe, E., Onodera, J., Harada, N., Honda, M. C., Kimoto, K., Kikuchi, T., Nishino, S., Matsuno, K., Yamaguchi, A., Ishida, A., and Kishi, M. J.: Enhanced role of eddies in the Arctic marine biological pump, Nature Comm., 5, 3950, doi:10.1038/ncomms4950, 2014.

Yamazaki, A., Inoue, J., Dethloff, K., Maturilli, M., and K nig-Langlo, G.: Impact of radiosonde observations on forecasting summertime Arctic cyclone formation, J. Geophys. Res., 120, doi:10.1002/2014JD022925, 2015.

Yang, J.: Seasonal and interannual variability of downwelling in the Beaufort Sea, J. Geophys. Res., 114, C00A14, doi:10.1029/2008JC005084, 2009.

Zhang, J., Spitz, Y. H., Steele, M., Ashjian, C., Campbell, R., Berline, L., and Matrai, P.: Modeling the impact of declining sea ice on the Arctic marine planktonic ecosystem, J. Geophys. Res., 115, C10015, doi:10.1029/2009JC005387, 2010.

Zhang, J., Lindsay, R., Schweiger, A., and Steele, M.: The impact of an intense summer cyclone on 2012 Arctic sea ice retreat, Geophys. Res. Lett., 40, 720–726, doi:10.1002/grl.50190, 2013.

Zhang, J., Ashjian, C., Campbell, R., Hill, V., Spitz, Y. H., and Steele, M.: The great 2012 Arctic Ocean summer cyclone enhanced biological productivity on the shelves, J. Geophys. Res., 119, 297–312, doi:10.1002/2013JC009301, 2014.

Table 1. Monthly mean values of NCEP/CFSR cloud fraction (n. d.), downward shortwave radiation ($W m^{-2}$), 10 m wind speed ($m s^{-1}$), snow depth (cm), sea ice thickness (cm), and sea ice concentration (n. d.) averaged in the NAP region. 2011 (2012) corresponds to the period from October 2010 (2011) to September 2011 (2012) to compare the model results.

		Oct	Nov	Dec	Jan	Feb	Mar	Apr	May	Jun	Jul	Aug	Sep
Cloud Fraction	2011	0.98	0.87	0.79	0.79	0.91	0.88	0.72	0.90	0.76	0.92	0.98	0.96
	2012	0.94	0.90	0.67	0.81	0.79	0.56	0.61	0.83	0.88	0.97	0.97	0.96
Shortwave Radiation	2011	9	0	0	0	4	51	165	236	305	217	102	45
	2012	10	0	0	0	4	62	170	245	264	184	92	46
Wind Speed	2011	6.7	5.1	5.0	5.1	6.0	4.3	4.6	4.4	4.5	4.4	5.3	5.4
	2012	8.1	5.0	4.8	5.1	4.7	4.5	4.1	3.9	4.7	4.7	7.1	7.1
Snow Depth	2011	11	23	32	37	41	44	46	33	0	0	0	0
	2012	8	23	22	21	23	23	22	13	0	0	0	0
Sea Ice Thickness	2011	60	209	216	261	276	281	268	249	228	169	78	0
	2012	60	210	232	271	279	278	286	259	207	141	62	0
Sea Ice Concentration	2011	0.21	0.89	0.98	0.99	0.99	0.99	0.99	0.99	0.99	0.83	0.19	0
	2012	0.19	0.90	0.98	0.98	0.98	0.98	0.99	0.97	0.87	0.70	0.18	0

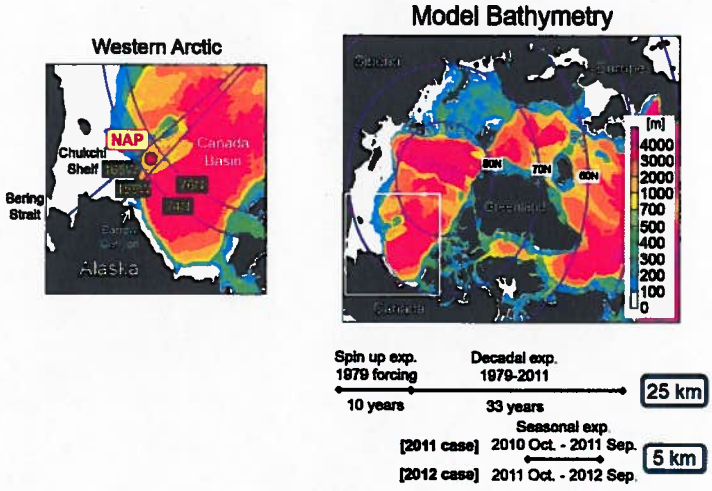

Figure 1. Bathymetry of the pan-Arctic sea ice–ocean model COCO. Location of Station NAP is indicated by a red dot in the left enlarged view. The NAP region defined in the present study is enclosed by 74–76° N and 159–165° W. Model integration period covers 33 years from 1979 to 2011 only for the physical oceanographic part using the 25 km resolution version, and the obtained fields are given as initial condition for one year experiment from October 2010 (2011) to September 2011 (2012) in the 2011 (2012) case using the 5 km resolution version with marine ecosystem components.

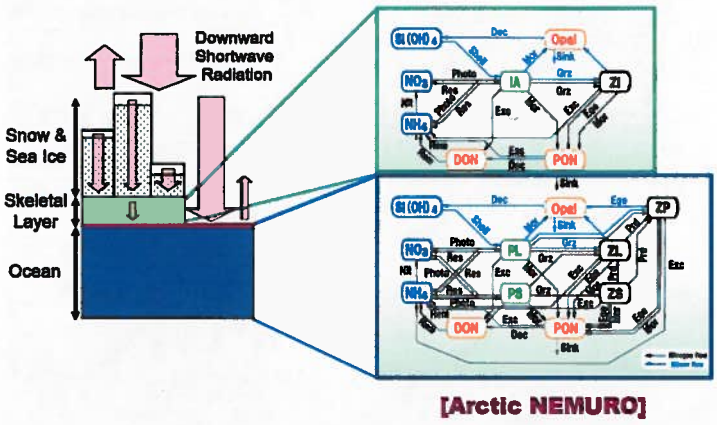

Figure 2. Schematic image and configuration of the Arctic NEMURO model. Nitrogen and silicon flows are composed of photosynthesis (Photo), shell formation (Shell), respiration (Res), excretion (Exc), mortality (Mor), grazing (Grz), predation (Prd), egestion (Ege), decomposition (December), remineralization (Rem), nitrification (Nit), sinking (Sink). Ice algal habitat is confined to the skeletal layer of sea ice bottom. Ice-related zooplankton (ZI) is neglected for simplicity in the present experiments. Exchange of biogeochemical variables with pelagic ecosystem is allowed at ice–ocean interface.

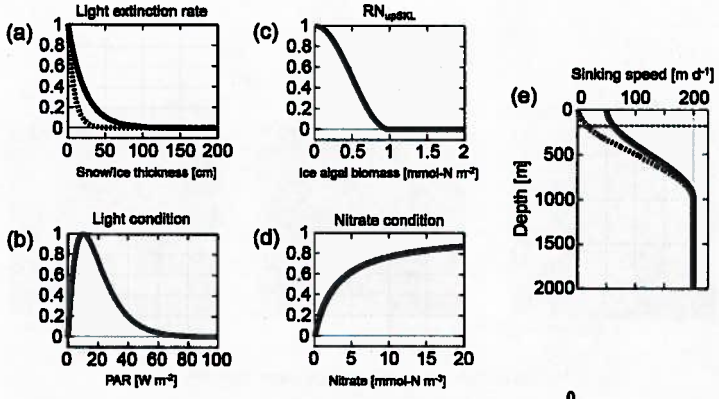

Figure 3. Relationships of **(a)** light extinction rate (non-dimensional (n. d.)) vs. thickness of (dashed line) snow and (solid line) sea ice (cm), **(b)** light condition term (n. d.) vs. light intensity (PAR) ($W m^{-2}$), **(c)** ice nutrient uptake ratio RN_{upSKL} (n. d.) vs. ice algal biomass ($mmol N m^{-2}$), **(d)** nitrate condition term (n. d.) vs. nitrate concentration ($mmol N m^{-3}$), and **(e)** sinking speed of PON derived from (solid line) ice algae and (dashed line) pelagic plankton groups ($m d^{-1}$) vs. depth in the water column (m), respectively, in the Arctic NEMURO model. See more information in Sect. 2.2.

Discussion Paper | Discussion Paper | Discussion Paper | Discussion Paper |

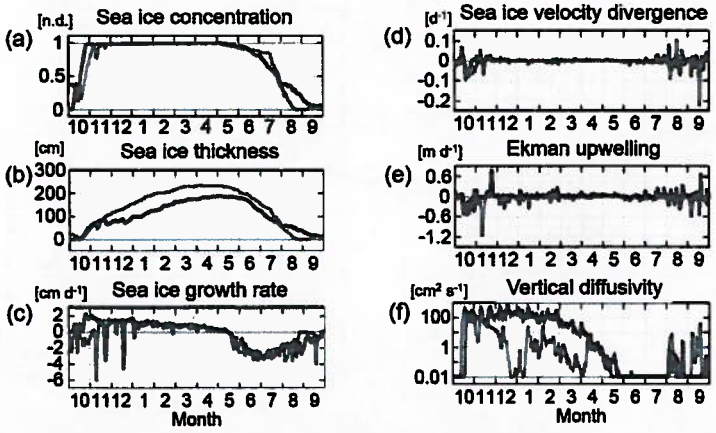

Figure 4. Seasonal transition of daily mean modeled variables in the NAP region. **(a)** Sea ice concentration (n. d.), **(b)** sea ice thickness (cm), **(c)** thermal growth rate of sea ice ($cm\,d^{-1}$), **(d)** divergence of sea ice velocity (d^{-1}), **(e)** Ekman upwelling velocity diagnosed using ocean surface stress fields ($m\,d^{-1}$), and **(f)** vertical diffusivity at the depth of 20 m ($cm^2\,s^{-1}$) in the (solid line) 2011 and (dashed line) 2012 cases. Note that negative values in **(c)**, **(d)**, and **(e)** correspond to sea ice melting, convergence of sea ice velocity, and Ekman downwelling, respectively. Vertical diffusivity in **(f)** is shown in a logarithm scale.

had to see what is dashed maybe use a grey or coloured line

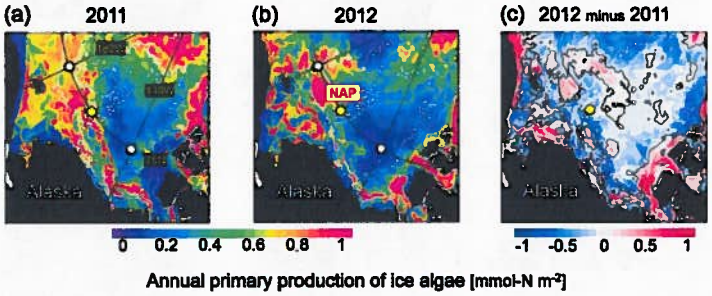

Figure 5. Modeled annual primary production of ice algae in the **(a)** 2011 and **(b)** 2012 cases ($mmol\,N\,m^{-2}$). The difference between two cases is shown in **(c)**. Yellow dots denote the location of Station NAP. White dots represent the eastern and western limits of 75° N section in Fig. 6b and c.

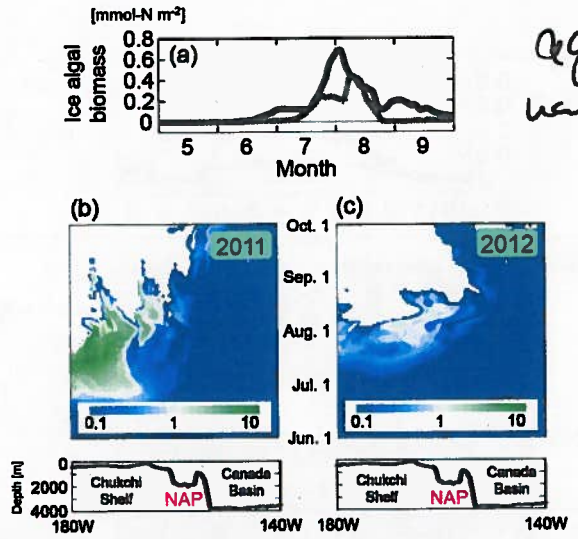

Figure 6. Modeled seasonal transition of ice algal biomass **(a)** in the NAP region and **(b, c)** along the 75° N line (mmol N m^{-2}). Sea floor depths along the east–west section are also plotted (m). Solid line in **(a)** and Hovm ller diagram in **(b)** correspond to the 2011 case. Dashed line in **(a)** and the diagram in **(c)** correspond to the 2012 case. The column content of 1 mmol N m^{-2} corresponds to the concentration of 50 mmol N m^{-3} when the skeletal layer thickness is set to 2 cm.

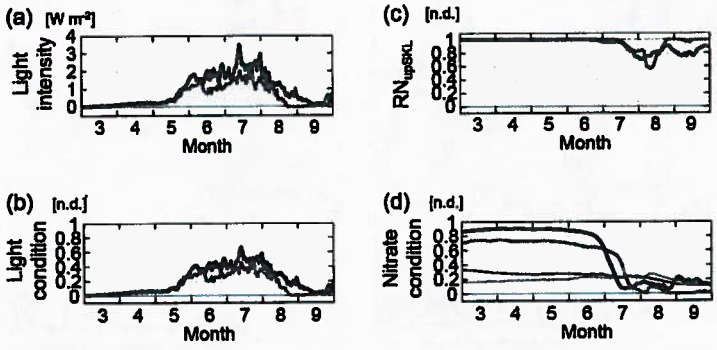

Figure 7. Modeled seasonal transition of **(a)** light intensity (PAR) in the skeletal layer (W m^{-2}), **(b)** light condition term (n. d.), **(c)** ice nutrient uptake ratio RN_{upSKL} (n. d.), and **(d)** nitrate condition term (n. d.) in the NAP region in the (solid line) 2011 and (dashed line) 2012 cases. Each term in **(b–d)** corresponds to ice algal value. In **(d)**, the condition terms in the (thick lines) skeletal layer and (thin lines) ocean surface layer are shown.

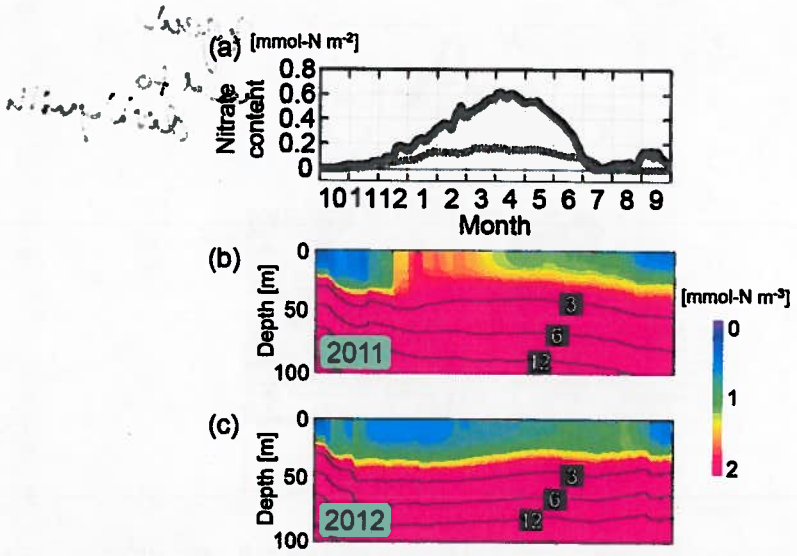

Figure 8. Modeled seasonal transition of nitrate concentration **(a)** in the skeletal layer (mmol N m^{-2}) and **(b, c)** in the top 100 m of water column (mmol N m^{-3}). Solid line in **(a)** and vertical profile in **(b)** correspond to the 2011 case. Dashed line in **(a)** and the profile in **(c)** correspond to the 2012 case.

Is PON the only obs. variable available for comparison? Does it show fit at all

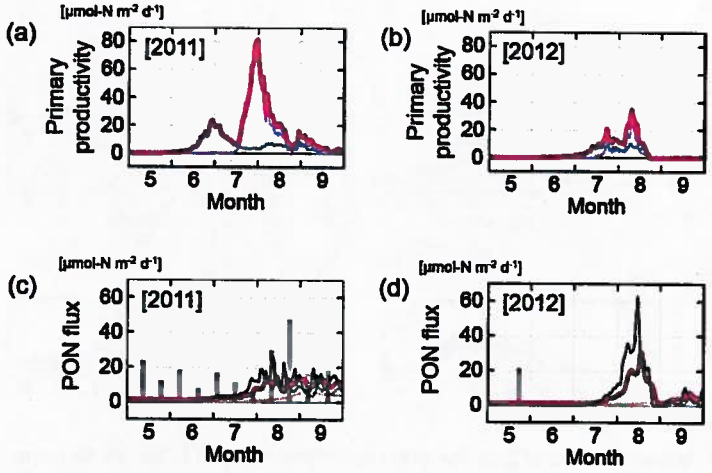

Figure 9. Modeled **(a, b)** primary production rate of ice algae and **(c, d)** PON flux in the NAP region in the **(a, c)** 2011 and **(b, d)** 2012 cases (μmol N m^{-2} d^{-1}). In **(a, b)**, the daily rate of primary production derived from nutrients in the (blue lines) skeletal layer and (pink lines) water column are also shown. In **(c, d)**, the total PON fluxes of (red lines) model outputs and (gray bars) trap values are compared at the depth of 180 m. The fluxes originating from (green lines) ice algae and (orange lines) pelagic plankton groups are also shown. The export flux from sea ice bottom to underlying water column is shown by black lines.

total simulated and observed

Scrittol
-> skeletal layer (blue line)
.... pelagic phytoplk. groups (orange line)

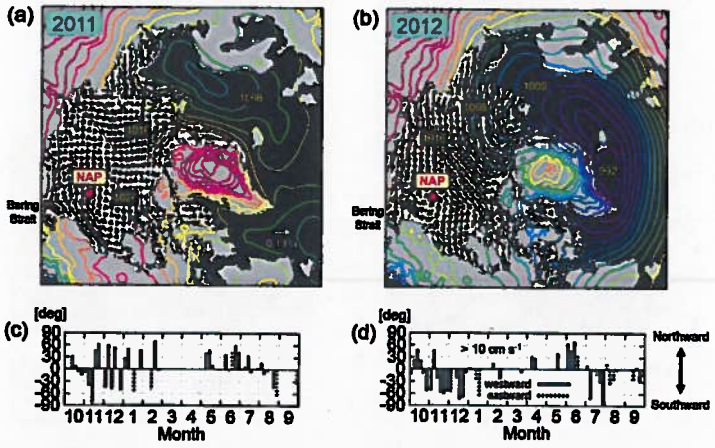

Figure 10. **(a, b)** (contours) Sea level pressure (SLP) (hPa) and (vectors) wind stress averaged **(a)** from November 2010 to January 2011 and **(b)** from November 2011 to January 2012. SLP is obtained from the NCEP/CFSR dataset, and wind stress vectors are calculated from the SLP field using the AOMIP formulation. Unit vector of wind stress is 0.1 Pa. **(c, d)** Direction of modeled sea ice velocity in the NAP region. Only five day averages whose velocity exceeds 10 cm s^{-1} in the **(c)** 2011 and **(d)** 2012 cases are plotted. Positive (negative) values of direction correspond to northward (southward), and solid (dashed) bars indicate westward (eastward) motions, respectively. For example, a solid bar of −45° means southwestward direction of 225° *T*.

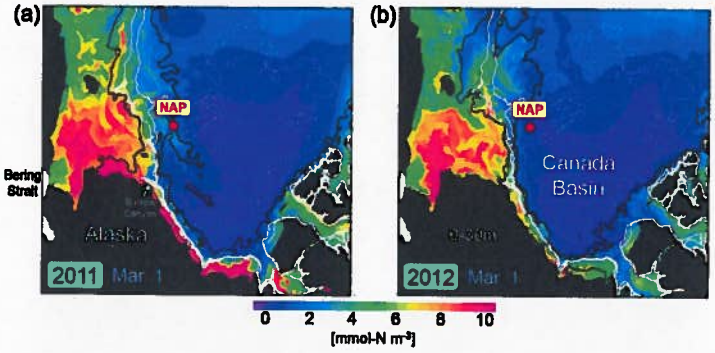

Figure 11. Modeled nitrate concentration averaged in the top 30 m of water column (mmol N m^{-3}). The daily mean fields on 1 March in the **(a)** 2011 and **(b)** 2012 cases are shown. In these experiments, a passive tracer is provided from the ocean surface to sea floor of 100–200 m depth along shelf-basin boundary sandwiched by thick white contours. Black contours correspond to a tracer value of 0.2 (0–30 m average). Thin white lines denote the isobaths of 100 and 3000 m.

Ok, sorry the white lines cannot be seen

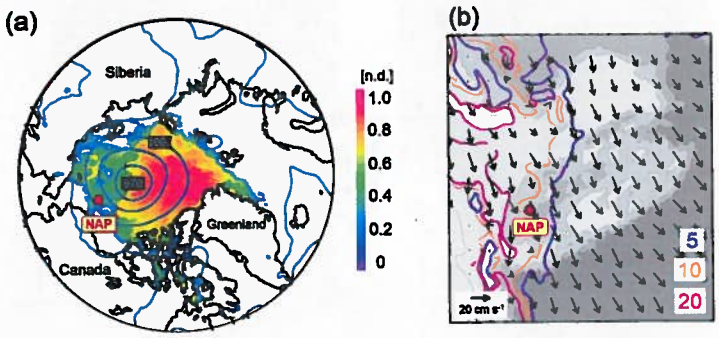

Figure 12. (a) NCEP/CFSR (contours) sea level pressure (hPa) and (shade) sea ice concentration (n. d.) on 6 August 2012. **(b)** Modeled (contours) PON flux at the depth of 180 m and (vectors) sea ice motion averaged for 3–10 August in the 2012 case. The flux contours of 5, 10, and 20 μmol N m^2 d^{-1} are shown around the Chukchi Borderland. The sea ice motion is overlaid every ten grid (i.e., approximately 50 km), and its unit vector is 20 cm s^{-1}. Red dots denote the location of Station NAP.